

# Quantum Transport Properties of Nanosized Ta<sub>2</sub>O<sub>5</sub> Resistive Switches: Variable Transmission Atomic Synapses for Neuromorphic Electronics

Tímea Nóra Török, Péter Makk, Zoltán Balogh, Miklós Csontos, and András Halbritter\*

Cite This: *ACS Appl. Nano Mater.* 2023, 6, 21340–21349

Read Online

ACCESS |

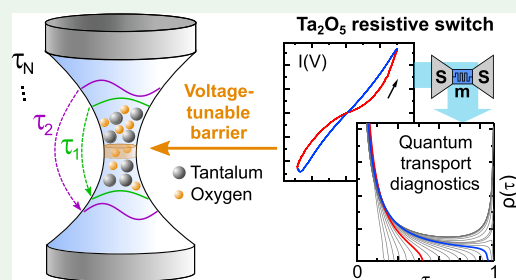
Metrics &amp; More

Article Recommendations

Supporting Information

**ABSTRACT:** Filamentary resistive switching (RS) devices are not only considered as promising building blocks for brain-inspired computing architectures but also realize an unprecedented operation regime where the active device volume reaches truly atomic dimensions. Such atomically sized RS filaments represent the quantum transport regime, where the transmission eigenvalues of the conductance channels are considered a specific device fingerprint. Here, we gain insight into the quantum transmission properties of close-to-atomic-sized RS filaments formed across an insulating Ta<sub>2</sub>O<sub>5</sub> layer through superconducting subgap spectroscopy. This method reveals the transmission density function of the open conduction channels contributing to the device's conductance. Our analysis confirms the formation of truly atomic-sized filaments composed of 3–8 Ta atoms at their narrowest cross-section. We find that this diameter remains unchanged upon RS. Instead, the switching is governed by the redistribution of oxygen vacancies or tantalum cations within the filamentary volume. The set/reset process results in the reduction/formation of an extended barrier at the bottleneck of the filament, which enhances/reduces the transmission of the highly open conduction channels. This transmission variability facilitates neuromorphic electronic applications in nanosized artificial synapses reaching the ultimate atomic scale.

**KEYWORDS:** random matrix theory, superconducting subgap spectroscopy, resistive switching, memristor, tantalum oxide



## INTRODUCTION

Resistive switching (RS) memory devices (a.k.a. “memristors”) are identified as a major hardware platform enabling the power-efficient implementation of artificial intelligence. Pioneering applications employ large memristor crossbar arrays in artificial neural networks, which implement machine learning approaches at the hardware level at unprecedented speed and energy efficiency.<sup>1–4</sup> The neuromorphic functionalities of single memristors arise from the dynamical properties of a previously unavailable operation regime, where the nanosized active device volume can reach truly atomic dimensions.<sup>5–9</sup> This ultrasmall active region is manifested by close-to-atomic-sized metallic filaments, which can be formed or ruptured by appropriate voltage signals. Such “artificial synapses” are utilized to encode synaptic weights through their analogue-tunable filamentary conductance.

Beyond the synaptic functionalities of RS devices, the metallic nature of the filamentary volume yields a completely different quantum transport regime compared to semiconductor heterostructures: (i) the large electron density ( $\approx 1$  electron/lattice atom) results in orders of magnitude larger Fermi energies ( $E_F^{\text{metal}} \approx 3\text{--}10\text{ eV}^{10}$ ) than in semiconducting systems. Therefore, quantum transport is realized at room temperature due to the  $E_F \gg k_B T$  condition. (ii) Unlike in semiconductor heterostructures, the metallic Fermi wavelength ( $\lambda_F^{\text{metal}} \approx 0.3\text{--}$

0.6 nm) falls in the regime of the lattice constant. Accordingly, the electrons experience a potential landscape that is rough on the scale of their wavelength. This results in far more complex quantum transport properties than universal conductance quantization in semiconductor quantum point contacts,<sup>11</sup> where a smooth, transparent quantum channel is realized. This complex quantum transport behavior has been widely investigated in pure metallic atomic-sized nanowires<sup>12–14</sup> but has remained poorly explored in filamentary RS devices.

In this paper, we investigate the quantum transport properties of nanoscale RS filaments formed across a Ta<sub>2</sub>O<sub>5</sub> thin film due to the voltage-induced redistribution of oxygen vacancies or tantalum cations.<sup>15,16</sup> Ta<sub>2</sub>O<sub>5</sub> is a prominent representative of transition metal oxides, which are widely considered a competitive material platform for neuromorphic hardware architectures.<sup>17–23</sup> In order to track the atomistic changes in the filament structure taking place upon RS, we

Received: October 6, 2023

Revised: October 30, 2023

Accepted: October 31, 2023

Published: November 15, 2023



apply superconducting subgap spectroscopy.<sup>5,12,14,24–26</sup> This method enables the analysis of the distribution of the  $\tau_i$  quantum transmission eigenvalues of the conduction channels, contributing to the conductance of the RS filament. The total filamentary conductance is obtained via the Landauer formula<sup>27</sup> as  $G = G_0 \sum_{i=1}^M \tau_i$ , where  $G_0 = 2e^2/h$  is the quantum conductance unit,  $M$  is the number of open conductance channels, and  $\tau_i$  is the probability of an electron crossing from one side to the other in the  $i$  eigenchannel. We focus on RS filaments, where  $M$  is sufficiently large so that the transmission eigenvalues can be described by a probability density function  $\rho^{\text{Ta}_2\text{O}_5}(\tau)$ . We determine  $\rho^{\text{Ta}_2\text{O}_5}(\tau)$  in the high (HCS) and low (LCS) conductance states and compare it to that of pure Ta nanowires,  $\rho^{\text{Ta}}(\tau)$ . Whereas a close-to-atomic-scale metallic nanowire is responsible for the conduction in both systems, the formation and environment of this metallic wire are fundamentally different. The reference Ta nanowires represent a pure metallic system that is thinned by mechanical elongation under vacuum conditions. In contrast, the oxide-based RS filaments are embedded in an insulating, amorphous  $\text{Ta}_2\text{O}_5$  matrix. The evolution of the RS junction relies on the voltage-induced displacement of oxygen vacancies and thereby the formation/destruction of oxygen-deficient conducting filamentary regions. Consequently, our analysis reveals a fundamentally different conductance channel distribution for the two systems. In pure Ta nanowires  $\rho^{\text{Ta}}(\tau)$  resembles the universal probability density function  $\rho^{\text{RMT}}(\tau) \sim \tau^{-1}(1-\tau)^{-1/2}$  in a broad diameter range. The latter formula was derived for mesoscopic diffusive wires by random matrix theory (RMT).<sup>28</sup> In this case, point-like scattering centers are considered, which are, however, bypassed by certain conductance channels, yielding almost perfect transmission ( $\tau_i \approx 1$ ) for a subset of the channels. In contrast, in RS filaments, the formation of an extended barrier across the narrowest section of the filament is revealed upon the reset transition, while the filament diameter is hardly affected. This barrier is attributed to the accumulation of oxygen ions. It reduces the transmission of the highly opened conduction channels, yielding a completely different transmission distribution than that of pure Ta nanowires. This observation highlights the role of a voltage-tunable transmission barrier at the device bottleneck, which enables the gradual tuning of the conductance weights even in atomic-sized artificial synapses.

## RESULTS AND DISCUSSION

**Experimental Approach.** For our comparative analysis, we established atomic-sized RS filaments in  $\text{Ta}_2\text{O}_5$  and pure Ta atomic wires by a STM (scanning tunneling microscopy) point contact setup and a mechanically controllable break junction (MCBJ) setup, respectively (see Figure 1a,c). In order to apply the method of superconducting subgap spectroscopy, both systems were cooled to a base temperature of  $T \approx 1.3$  K, which is well below the superconducting phase transition of tantalum ( $T_C = 4.48$  K). The current–voltage [ $I(V)$ ] characteristics of a statistical ensemble of junctions were recorded in the superconducting state and fitted by simulated  $I(V)$  curves relying on model transmission distributions. In the following, we describe our experimental approach. Next, we discuss the applied model transmission distributions and the fitting procedure. Finally, we describe and discuss the results of our analysis.

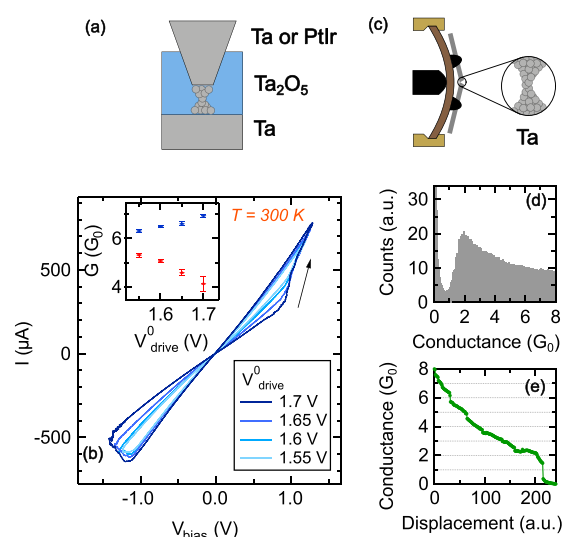


**Figure 1.** Characterization of RS filaments in  $\text{Ta}_2\text{O}_5$  and pure Ta atomic wires. (a) Illustration of a  $\text{Ta}_2\text{O}_5$  RS device realized in a STM point-contact arrangement. (b) Representative room temperature RS current–voltage characteristics using a conventional PtIr tip. The hysteretic switching trace opens up as the amplitude of the triangular driving voltage signal is increased (see the color-scale). Arrow indicates the direction of the hysteresis. The inset shows the low-bias conductance of the HCS (blue) and LCS (red) at each voltage amplitude, demonstrating multilevel programming (average and standard deviation of 10 consecutive switching cycles are shown for each voltage). (c) Illustration of pure Ta atomic wires established by mechanical rupture using the three point bending arrangement in a MCBJ setup. (d) Representative conductance histogram of pure Ta nanowires obtained by collecting thousands of conductance vs electrode separation traces during the repeated opening and closing of the junction. The cryogenic vacuum at liquid helium temperature grants extreme cleanliness during the in situ rupture. (e) Exemplary conductance vs electrode separation trace.

RS was studied in a STM point-contact setup, which was shown to be an efficient method in the investigation of memristive filaments.<sup>5,29–46</sup> Prior STM or conductive AFM studies on electrochemical metallization cells<sup>29–31,38,40–46</sup> and transition metal oxide systems<sup>5,32,33,36,37,39,42</sup> applied either gap-type arrangements,<sup>31,35–38</sup> where the filament is grown to the airgap between the surface and the tip, or a gapless arrangement,<sup>5,29,30,32,33,39–46</sup> where the tip is indented to the surface. Here, we apply the latter method, which grants proper mechanical stability for the STM break junction to withstand similar voltage and current levels<sup>5,29,30,32,33,39–46</sup> as conventional nanofabricated devices. In our study, PtIr or Ta tips were approached and touched to  $\text{Ta}_2\text{O}_5/\text{Ta}$  thin film samples in a controlled manner. The PtIr tips were applied in routine room temperature characterization measurements using the same experimental apparatus as in ref 39. The Ta tips were used in the low temperature measurements (see ref 5 for the experimental methods) to have superconducting electrodes at both sides of the RS filament. STM geometry is ideal for the application of superconducting spectroscopy as bulk superconducting electrodes can be realized and pushed very close to each other. In this case, the tip-sample geometric asymmetry ensures stable RS<sup>43</sup> despite the electrode materials being the same. Such STM point-contact samples exhibit similar characteristics as conventional cross-point samples created with an electron beam lithography technique (see Supporting Information, Figure S1). The RS layer was prepared by

sputtering  $\sim 30$  nm thick stoichiometric Ta<sub>2</sub>O<sub>5</sub> on top of a 30 nm thick Ta layer. The thickness and composition of the Ta<sub>2</sub>O<sub>5</sub> layer were confirmed by X-ray photoelectron spectroscopy (XPS) measurements accompanied by Ar<sup>+</sup> ion milling, which yielded identical results as the data presented in our previous work using similarly prepared Ta<sub>2</sub>O<sub>5</sub> samples (Figure 1d in ref 39). However, the composition of the active layer might be different than the 2:5 ratio observed near the top since the tip is indented to the Ta<sub>2</sub>O<sub>5</sub> layer and switching takes place close to the Ta<sub>2</sub>O<sub>5</sub>/Ta interface, where the results of XPS are less conclusive due to the smearing effects of ion milling. A vital part of creating a STM point-contact sample is the controlled approach of the tip to the surface of the thin layer sample with a given set point resistance. According to our past experiences with the STM point-contact technique,<sup>5,39–46</sup> this process leads to electroforming-free RS samples since the tip can be indented to the surface of the RS material. To avoid the bending of the tip during the indentation, robust Ta and PtIr wires with 1 and 0.25 mm diameter were used, ensuring a short free-standing part and avoiding long and narrow tip apexes by the proper scissor cutting. During the controlled tip-approaching process, the sample was biased at  $\sim 20$  mV, and feedback was applied to the tip-sample resistance. The approach was terminated when an  $\sim$ nA current was detected, resulting in less than  $\sim 20$  M $\Omega$  resistance. Afterward, the  $I(V)$  characteristics with typical voltage driving amplitudes of  $V_{\text{drive}}^0 \approx 1\text{--}2$  V readily exhibited RS without a dedicated high voltage electroforming process. In comparison, the pristine resistance of on-chip Pt/Ta<sub>2</sub>O<sub>5</sub>/Ta cross-point samples with an oxide layer thickness of 3.5 nm (see examples for their RS behavior in the Supporting Information, Figure S1) was typically much greater than the  $\sim 20$  M $\Omega$  value of pristine STM point-contacts, which suggests that the tip was indented deep into the oxide layer, resulting in a  $< 3.5$  nm thin active region (see Figure 1a). The similarities of the RS  $I(V)$  characteristics to those measured on Pt/Ta<sub>2</sub>O<sub>5</sub>/Ta cross-point samples (see Supporting Information, Figure S1) also imply that the thicknesses of the active regions (as well as the switching mechanisms) are very similar in the two cases.

During  $I(V)$  measurements, the set process was terminated by a series resistor of  $R_s = 300\text{--}3600$   $\Omega$ . Accordingly, the bias voltage on the sample is calculated as  $V_{\text{bias}} = V_{\text{drive}} - IR_s$ . The details of the switching were fine-tunable by either the gentle manipulation of the STM tip or the variation of the driving voltage amplitude. Room temperature RS characteristics at a fixed tip position and varying driving amplitude are exemplified in Figure 1b. Positive bias refers to a higher potential acting on the thin film with respect to the STM tip. The observed  $I(V)$  characteristics are similar to those reported in the literature in various tantalum oxide-based filamentary systems.<sup>20,47</sup> The filaments formed during RS are composed of metal cations or oxygen vacancies. There are several microscopic processes that can cause filamentary RS behavior in valence change memories. Besides the migration and valence change of oxygen vacancies,<sup>48</sup> the movement of metal cations can also account for RS, according to first-principle simulations<sup>49–51</sup> and experiments.<sup>36</sup> The inset of Figure 1b shows the low-bias conductance values in the LCS and HCS of the hysteretic  $I(V)$  characteristics demonstrating fine analogue tunability in the  $4G_0\text{--}7G_0$  range. Recently, thousands of stable conductance levels were demonstrated in metal oxide-based memristors in the range of  $0.5G_0\text{--}50G_0$ ,<sup>52</sup> which is a standard operation regime for redox-based filamentary RS devices.<sup>53–59</sup> Our

measurements on several RS junctions focused on this typical conductance regime for filamentary devices,  $\approx 1G_0\text{--}15G_0$ , where the quantum transport properties can be compared with those of atomic-sized pure tantalum nanowires. Measurements utilizing Ta STM tips exhibited similar characteristics both at room temperature (see Figure S1 in the Supporting Information) and at cryogenic temperatures (the latter is demonstrated later in the section describing the Results of the Subgap Spectroscopy Measurements). Note that the above conductance regime is also ideal for RS synapses in artificial neural networks, where high-accuracy hardware-based vector-matrix multiplication operations require linear  $I(V)$  characteristics below the RS threshold voltage.<sup>1,2,54</sup>

As a reference system, we have established pure Ta atomic-sized wires in a MCBJ arrangement. In this setup, a notched Ta wire with a 0.1 mm diameter is broken in a three point bending configuration (see Figure 1c) using the combination of a coarse stepper motor actuation and a fine piezo control. To characterize such established Ta nanowires, thousands of conductance vs electrode separation traces (see an example trace in Figure 1e) are recorded along the repeated opening and closing of the junction. The conductance data of these traces are used to construct a conductance histogram (Figure 1d). Note that both the voltage controlled RS filaments (see Figure 1b and a further example covering the  $\approx 1G_0\text{--}3G_0$  regime in Figure S2 of the Supporting Information) and the mechanically actuated pure Ta nanowires exhibit a fine analogue tunability of the conductance in the entire investigated conductance range, lacking any conductance quantization features.

The  $I(V)$  characteristics of the superconductor (S)–nanoconstriction (c)–superconductor (S) junctions were acquired according to the same protocol as in our previous work on the subgap analysis of niobium-oxide RS filaments.<sup>5</sup> The latter work focused on the investigation of RS filaments with a truly single-atom cross-section dominated by a single conductance channel. That study provides a proof-of-principle methodology for investigating single-atom junctions in the vicinity of  $G_0$  conductance. Here, we investigate somewhat broader RS filaments with significantly more open conductance channels, where the in-depth analysis of the probability density of transmission eigenvalues,  $\rho(\tau)$ , and the comparison to model transmission densities provide new information on quantum transport phenomena in broader RS filaments up to several atoms. We exploit the fact that in a ScS junction, the current contributions of multiple Andreev reflection processes strongly depend on the corresponding transmission eigenvalues. Consequently, the superconducting  $I(V)$  characteristics provide a sensitive diagnostic tool to investigate  $\rho(\tau)$  (see the computed ScS  $I(V)$  curves in Figure S3 of the Supporting Information).

### Model Analysis of the Transmission Distributions.

Our modeling approach for the fitting of the superconducting  $I(V)$  characteristics is illustrated in Figure 2. As a reference, we rely on the  $\rho^{\text{RMT}}(\tau) \sim \tau^{-1}(1 - \tau)^{-1/2}$  universal probability density function of the transmission eigenvalues (see the brown curve in Figure 2b). This density function was derived for phase-coherent mesoscopic diffusive wires with a large number of open conductance channels ( $M \gg 1$ ). The corresponding model system is illustrated in the second panel of Figure 2a (brown frame), where the gray background symbolizes the diffusive nature of the transport. The RMT density function is bimodal:  $\rho^{\text{RMT}}(\tau)$  is peaked at both the low-

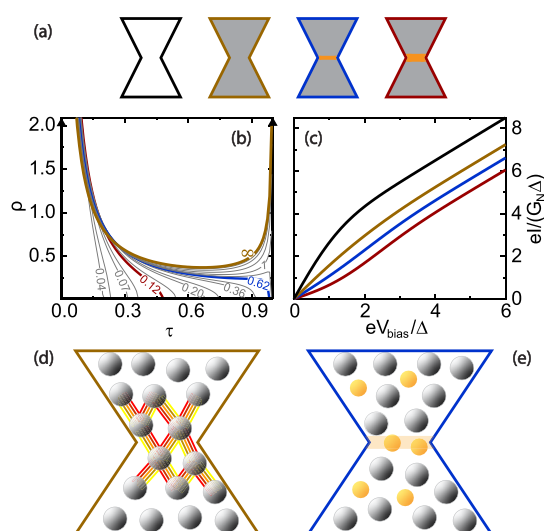


**Figure 2.** Model approach for the analysis of the quantum conductance channel distributions. Panel (a) illustrates possible model geometries: (i) a ballistic quantum wire (black frame), (ii) a diffusive wire without any extended barrier (brown frame), and (iii) a diffusive wire with a weaker/stronger extended barrier at the bottleneck (blue/red frame). The corresponding model transmission density functions are illustrated in panel (b): the black Dirac delta peaks illustrate the case of quantized conductance channels in a ballistic quantum wire. The brown curve shows the  $\rho^{\text{RMT}}(\tau)$  density function for a diffusive wire. The gray curves, including the blue/red example curves, represent the density functions in the case of an extended barrier with variable strength, as labeled by the  $\alpha$  parameters. Panel (c) shows the calculated ScS  $I(V)$  curves at  $G = 10G_0$  for  $\rho^{\text{RMT}}(\tau)$  (brown), for a filament with a weaker/stronger-extended barrier (blue/red curves corresponding to the blue/red density functions highlighted in panel (b)), and for a highly transparent junction with perfectly open conductance channels (black). In the latter case, an ideally infinite zero bias slope is expected. Apparent finite slope is a result of the finite energy resolution included in our model. Panels (d,e), respectively, illustrate a pure Ta atomic wire and an oxide-based RS filament. In (d), the five colored lines connecting two neighboring atoms illustrate the typical transport through 5 nonvanishing interatomic conductance channels in a d-valent metal. The transmission eigenvalues of such 5 interatomic channels strongly scatter between zero and unity transmission, giving rise to a diffusive-like transport. In the oxide-based RS filaments (e), the relocation of oxygen atoms plays a key role in the switching process, also influencing the transport properties. The eventual formation of an extended barrier (as illustrated by the orange region) is attributed to the voltage-controlled accumulation of oxygen. Note that panels (d,e) are artistic illustrations, where the hourglass shape emphasizes a key aspect of atomic-sized wires: the behavior of such wires is always dominated by the region, where the wire cross-section is the narrowest<sup>12</sup> as the major part of the voltage drops in this region, and the current density as well as the self-heating are also the largest in this region.

transmission ( $\tau \ll 1$ ) and high-transmission ( $\tau \approx 1$ ) ends, while the intermediate region also exhibits a finite weight. The presence of completely open conductance channels, which was indeed confirmed by shot noise measurements,<sup>60</sup> seems counterintuitive due to the diffusive nature of the transport, that is, the short mean free path compared to the system size. However, it can be shown that point-like defects can be bypassed by certain conductance channels, yielding almost perfect channel transmission.<sup>28</sup> It was recognized that this universal density function also well approximates the trans-

mission distribution in Pb atomic-sized wires,<sup>61</sup> where the disordered nature is attributed to the interplay of nonperfect crystalline ordering, nonperfect transmission, especially through the highly oriented p orbitals, and surface scattering. We anticipate similar behavior in transition metals, like the investigated pure Ta nanowires, where the electron transmission through two neighboring atoms is shared among  $\approx 5$  conductance channels, as illustrated by the 5 colored lines between two neighboring atoms in Figure 2d. This expectation relies on the tight-binding model of a single-atom nanowire<sup>13,62</sup> identifying the number of channels with the number of valence orbitals at the central atom (i.e., 1 s-type and 5 d-type channels in a transition metal) and predicting the closing of one channel due to symmetry reasons. This specific behavior was experimentally verified in Nb and Ta junctions, which have very similar electron structures and conduction properties.<sup>14,26</sup> Note that the above considerations imply  $\approx 10$ – $15$  nonvanishing conductance channels for a filament with only 2–3 atoms in its narrowest cross-section. Such a large channel number justifies the applicability of a transmission density function.

Our goal is to experimentally verify the universal transmission density function in pure Ta atomic wires and to identify and understand possible deviations from this in oxide-based RS filaments. The presence of oxygen near a metallic atomic wire can have profound effects on its transport properties in various ways. Oxygen ions may form an extended barrier or individual point-like defects, affecting quantum transport properties. They can also block transport in the d orbitals, enhancing the dominance of the s channel, resembling the phenomenon experimentally demonstrated in nickel atomic wires in the presence of oxygen.<sup>63</sup> The latter would yield a more transmissive situation compared to  $\rho^{\text{RMT}}(\tau)$ , whereas the formation of an extended barrier would yield a less transmissive situation. Since the (re)distribution of oxygen impurities and/or metal cations (see Figure 2e) plays important roles both in the transport properties and in the RS process, a quantitative comparison of RS filaments and pure Ta atomic wires will enable one to draw conclusions about the atomic-scale evolution of the filament upon RS. To this end, we consider possible model transmission density functions with both *more transmissive* and *less transmissive* characteristics (see Figure 2a,b). In the former case, the most extreme situation is illustrated: a fully ballistic junction (left panel in Figure 2a, where the white background symbolizes the ballistic nature). This scenario corresponds to the case of universal conductance quantization, where all open conductance channels exhibit perfect transmission, as demonstrated by the black density function with Dirac-delta peaks at  $\tau = 0$  and 1 in Figure 2b. The situation where the overall transmission is lowered compared to the RMT case can be considered according to the model of Nazarov<sup>64</sup> where an extended barrier is formed at the bottleneck of the filament. This results in an enhanced backscattering in all the channels, yielding a suppression of the peak at  $\tau \approx 1$  in the  $\rho^{\text{RMT}}(\tau)$  transmission distribution. This model relies on the series connection of a diffusive wire with  $R_W$  resistance and an extended barrier with  $R_B$  resistance. The correspondingly derived transmission density function depends on the  $\alpha = R_W/R_B$  parameter, as demonstrated by the gray curves (including the example curves highlighted in red and blue) in Figure 2b. The corresponding model systems are illustrated in the right two panels of Figure 2a, where the orange region symbolizes the extended barrier.

Note that the  $\alpha \rightarrow \infty$  limit recovers the universal  $\rho^{\text{RMT}}(\tau)$  transmission density function.

In order to experimentally determine the relevance of the scenarios described above in our devices, we compare the measured  $I(V)$  traces to the simulated model  $I(V)$  traces corresponding to a given transmission density function as follows. By choosing a certain model transmission density function  $\rho(\tau)$  normalized to unity ( $\int \rho(\tau) d\tau = 1$ ), the average transmission probability of the open channels is determined as  $\bar{\tau}_\rho = \int \tau \rho(\tau) d\tau$ . Relying on this average transmission, the number of open channels at a certain  $G$  conductance is estimated as  $M_{\rho,G} = \text{round}((G/G_0)/\bar{\tau}_\rho)$ . The transmission eigenvalues of an atomic filament/wire with  $G$  conductance are simulated by generating  $M_{\rho,G}$  random numbers according to the chosen  $\rho(\tau)$  probability density function. Having these random transmission eigenvalues at hand, the  $I(V)$  curve of the hypothetical ScS junction characterized by the particular  $\tau_i$  values is simulated according to the multiple Andreev reflection theory.<sup>61,65,66</sup> For the sake of a meaningful comparison to experimental  $I(V)$  data, ensemble averaging is performed by repeating the above approach for a large number of independent sets of random transmission eigenvalues. Thereby, an average ScS  $I(V)$  characteristic can be modeled.

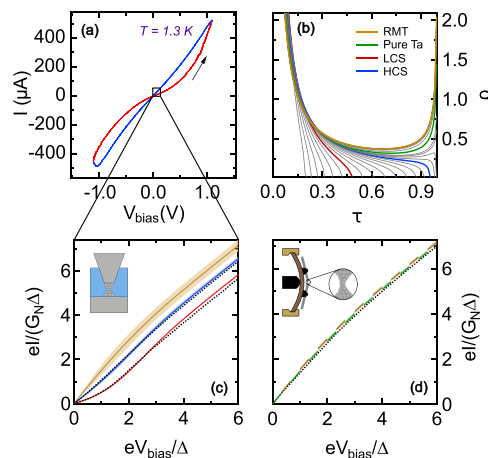
Additionally, our analysis also takes into account the finite energy resolution of the measurements arising from the proximity effect<sup>5</sup> by smoothing the modeled  $I(V)$  curves with a Gaussian kernel according to the actual energy resolution (see further details in Figure S3 of the Supporting Information). Furthermore, our numerical analysis applies a bottom cutoff at  $\tau = 0.03$ , that is, channels with smaller transmission are not considered open. With this physically reasonable choice  $\rho^{\text{RMT}}(\tau)$  yields  $\bar{\tau}_\rho = 0.39$ , which reproduces the expected  $M = 5$  open channels for a single-atom junction corresponding to the conductance histogram peak in Figure 1d. The value of  $\bar{\tau}_\rho$  and  $M$  obviously depends on the choice of the cutoff, but the results of the subgap analysis are insensitive to the precise cutoff value (see Figure S4 of the Supporting Information).

Figure 2c shows such simulated  $I(V)$  characteristics for hypothetical ScS junctions with  $G = 10G_0$  conductance and various transmission density functions. The brown curve illustrates the case of the universal  $\rho^{\text{RMT}}(\tau)$  density function corresponding to the brown curve in Figure 2b. The blue and red curves correspond to junctions including extended barriers with  $\alpha = 0.62$  and  $\alpha = 0.12$ , respectively (see the blue and red  $\rho(\tau)$  curves in Figure 2b). As a reference, the black curve corresponds to a junction satisfying universal conductance quantization, where all of the open conductance channels have  $\tau_i = 1$  transmission. The ScS  $I(V)$  trace shows markedly different behavior for the above fundamentally different transmission densities. By normalizing the  $I(V)$  curves with the  $\Delta$  superconducting gap and the  $G_N$  normal state conductance (see the axes in Figure 2c), a unity slope line is obtained in the normal state for any filament type. Superconductivity, however, enhances the contribution of open channels ( $\tau_i \approx 1$ ) and suppresses the contribution of weakly transmitting channels ( $\tau_i \ll 1$ ). Accordingly, a junction with highly/poorly transmitting channels (black/red) exhibits a considerably larger/smaller slope than unity around zero bias ( $eV \ll 2\Delta$ ). As another dominant difference, the highly transmitting junction also exhibits a considerable excess current; that is, the high-bias linear section of the  $I(V)$  curve

extrapolates to a significant positive current at zero bias.<sup>67</sup> The universal  $\rho^{\text{RMT}}(\tau)$  density yields an  $I(V)$  curve between these two extremities, with a moderately larger than unity slope at zero bias and a moderate excess current at high bias.

### Results of the Subgap Spectroscopy Measurements.

Figure 3 displays the subgap analysis of the transmission



**Figure 3.** Subgap analysis of the conductance channels in a representative RS filament and a pure Ta atomic wire. (a) Typical RS curve of Ta(tip)/Ta<sub>2</sub>O<sub>5</sub>/Ta STM junctions at a cryogenic temperature. Arrow indicates the direction of the hysteresis. (b) The red, blue, and green lines demonstrate the best-fitting transmission densities for the LCS and HCS of the RS filament in panel (c) and for the pure Ta atomic wire in panel (d), respectively. As a reference, the light brown curve shows  $\rho^{\text{RMT}}(\tau)$ . (c) ScS  $I(V)$  curves for their HCS (top dotted line,  $G = 4.03G_0$ ) and the LCS (bottom-dotted line,  $G = 2.02G_0$ ) of the RS  $I(V)$  curve in panel (a). The blue and red curves represent the best-fitting model  $I(V)$  curves, whereas the light brown curve shows the model  $I(V)$  curve for  $\rho^{\text{RMT}}(\tau)$  as a reference. For all the colored curves, the light-colored background region represents the standard deviation of the  $I(V)$  curves for the same density function but various random transmission sets. (d) Measured ScS  $I(V)$  curve (dotted line,  $G = 8.33G_0$ ) and the best-fitting model  $I(V)$  curve (green dashed line) for the reference pure Ta atomic wire. Measured  $I(V)$  curve very much resembles the model  $I(V)$  curve for  $\rho^{\text{RMT}}(\tau)$  (light brown dashed line).

density functions based on the ScS  $I(V)$  curves measured on RS filaments (Figure 3c) and pure Ta atomic wires (Figure 3d). As a reference, first the data of the latter system is analyzed. The dotted line shows the measured ScS  $I(V)$  curve, which very much resembles the simulated  $I(V)$  curve according to the universal  $\rho^{\text{RMT}}(\tau)$  density function (brown dashed line). A slightly better agreement is obtained according to Nazarov's theory,<sup>64</sup> using the best fitting  $\alpha = 1.6$  parameter (green dashed line). The corresponding transmission density function (green line in Figure 3b) is indeed positioned very close to the  $\rho^{\text{RMT}}(\tau)$  universal density function (brown curve in Figure 3b). This analysis supports our preconception that Ta atomic wires are well described by the universal transmission density function. For this particular junction, the  $G = 8.33G_0$  conductance and the universal transmission density function yield  $M \approx 21$  open channels, indicating a junction with  $\approx 4$  atoms at the narrowest cross-section according to the 5 channels/atom estimate.

Figure 3a exemplifies a cryogenic temperature ( $T \approx 1.3$  K) RS curve, where the HCS and LCS are shown in blue and red colors, respectively. RS occurs on the voltage-scale of 1 V,

whereas the superconducting features are detected on a much smaller voltage scale,  $V \approx 2\Delta/e \approx 1.33$  mV.<sup>68</sup> The top and bottom dotted lines in Figure 3c show the measured ScS  $I(V)$  curves in the latter voltage range for the HCS and the LCS, respectively. The blue and red lines represent the best-fitting model  $I(V)$  curves according to Nazarov's theory, using  $\alpha = 0.51$  (HCS, blue curve) and  $\alpha = 0.12$  (LCS, red curve). The corresponding transmission density functions are shown in Figure 3b by blue and red lines, respectively. These density functions, especially the red curve for the LCS, significantly differ from the light brown universal density function,  $\rho^{\text{RMT}}(\tau)$ . This significant difference is also demonstrated at the level of the ScS  $I(V)$  curves in Figure 3c. The brown curve shows the reference average  $I(V)$  curve corresponding to  $\rho^{\text{RMT}}(\tau)$ , such that the light brown region marks the standard deviation of the  $I(V)$  curve for different random number transmission sets. Similarly, the light blue and light red regions for the blue and red model  $I(V)$  curves demonstrate the standard deviation of these  $I(V)$  curves for different random number sets, though for the red curve, this standard deviation is so small that it is not visible on the curve. It is clear that the deviation of the HCS and LCS  $I(V)$  traces from the reference brown curve calculated with  $\rho^{\text{RMT}}(\tau)$  is significantly larger than the standard deviation of the model  $I(V)$  curves.

Figure 4a displays the results of the statistical analysis performed for a larger amount of oxide-based RS filaments

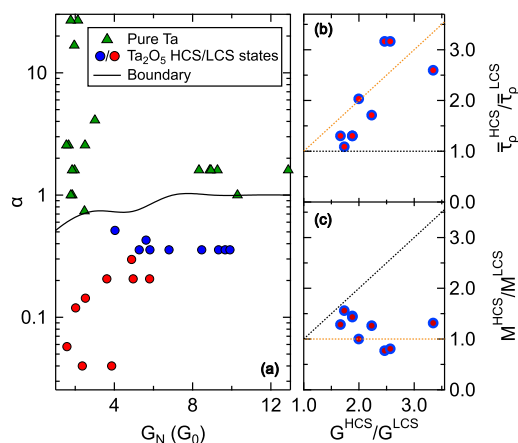


**Figure 4.** Analysis of the barrier strength for a statistical ensemble of pure Ta nanowires and RS filaments. (a)  $\alpha$  Values extracted from the ScS  $I(V)$  curve fitting are presented for multiple pure Ta atomic wires (green triangles) as well as the HCS (blue dots) and LCS (red dots) states of various RS filaments. The black line demonstrates the border above/below which the deviation from the  $\rho^{\text{RMT}}(\tau)$  universal transmission density function is insignificant/significant. Panels (b,c), respectively, demonstrate the average transmission ratio and the channel number ratio as a function of the conductance ratio for all the RS transitions in panel (a). The orange/black dotted line illustrates the cases where solely the transmission/channel number changes during reset.

(blue circles for the HCS and red circles for the LCS) as well as for several pure Ta atomic wires (green triangles) covering the conductance range of  $\approx 1$ – $13G_0$ . The  $\alpha$  parameter of the model density functions is extracted by fitting the ScS  $I(V)$  curves, likewise in Figure 3. The black curve represents a quantitative boundary as a function of conductance. Below this boundary, the standard deviation of the best-fitting model  $I(V)$  curve does not overlap with the standard deviation of the

model  $I(V)$  curve corresponding to  $\rho^{\text{RMT}}(\tau)$ . That is, below this boundary line, the density function best describing the measured ScS  $I(V)$  curve significantly differs from  $\rho^{\text{RMT}}(\tau)$ . Figure 4 shows that all the measurements on pure Ta atomic wires/oxide-based RS filaments show a nonsignificant/significant difference compared to the  $\rho^{\text{RMT}}(\tau)$  density function. Furthermore, it is also clear that in the LCS of the RS filaments (red circles), the deviation from  $\rho^{\text{RMT}}(\tau)$  is even more pronounced than in the HCS (blue circles).

## DISCUSSION

Finally, we discuss the results of our superconducting subgap analysis. First, we have confirmed our preconception that the quantum transport in pure Ta atomic-sized nanowires is well described by  $\rho^{\text{RMT}}(\tau)$ . Moreover, this universal transmission density is valid over the entire investigated conductance range (see Figure 4). As the Ta wire is elongated, the number of open channels decreases, but the characteristic distribution of the transmission eigenvalues and, thereby, the  $\bar{\tau}_p \approx 0.39$  average transmission is left similar. The  $\rho^{\text{RMT}}(\tau)$  density function represents a broad variation of the transmission eigenvalues with some highly open channels. We attribute the latter to the transmission through s-type orbitals, whereas the d-type orbitals rather contribute to the broad variation of  $\tau_i$ . Despite the few open channels,  $\rho^{\text{RMT}}(\tau)$  does not yield any sign of conductance quantization features, as demonstrated by the simulated conductance histogram in Figure S4 of the Supporting Information. This is in sharp contrast to noble metals and alkali metals, where a significantly more transmissive transmission density function<sup>69</sup> is realized due to the dominance of the highly delocalized s-electrons and, thus, conductance quantization is observed.<sup>13,14</sup>

In filamentary RS devices, the formation of atomic-sized metallic filaments is anticipated, where quantum transport properties might resemble those of pure metallic nanowires. Our analysis, however, highlights significant differences. The superconducting excess current<sup>67</sup> and the leading subgap contribution to the ScS  $I(V)$  curve are quadratically suppressed for  $\tau \ll 1$ , that is, these superconducting features are extremely sensitive to the presence of transparent channels, even if they represent a minority in the entire distribution. This enables the precise identification of the weak barrier described by  $\alpha$ , from which the average transmission values and the corresponding number of open channels can be determined. For the representative switching curve in Figure 3a,c, this analysis yields  $\bar{\tau}_p = 0.25$  and  $M = 16$  in the HCS and  $\bar{\tau}_p = 0.12$  and  $M = 17$  in the LCS. These results evidence a markedly different scenario compared to pure Ta nanowires: in the RS filament, the reset transition leaves the number of open channels nearly unchanged. Instead, the resistance change occurs due to a significant decrease in the average transmission. Such a process is consistent with the atomistic picture of the RS mechanism, where the electric field-driven redistribution of oxygen ions or tantalum cations at the filament bottleneck (see the schematic illustration in Figure 2e) results in a stronger/weaker transport barrier in the LCS/HCS, whereas the overall diameter of the filament stays similar. The unchanged filament diameter and modulated oxygen vacancy concentration upon the reset transition are also in qualitative agreement with continuum model simulations performed in the limit of nanometer-scale RS filaments in TaO<sub>x</sub>-based memristors.<sup>16</sup> Our analysis yields an estimate on the filament size, assuming that the 5 channels

between two neighboring Ta atoms are a reasonable assumption for the oxide-based RS filaments as well. According to this assumption, the HCS and LCS in Figure 3a,c correspond to a RS filament with  $\approx 3$  Ta atoms in the narrowest cross-section, with smaller/larger oxygen content in the HCS/LCS bottleneck.

To perform similar analysis on various RS junctions, we plot the  $\bar{\tau}_\rho^{\text{HCS}}/\bar{\tau}_\rho^{\text{LCS}}$  (Figure 4b) and the  $M^{\text{HCS}}/M^{\text{LCS}}$  (Figure 4c) ratios as a function of the  $G^{\text{HCS}}/G^{\text{LCS}}$  conductance ratio for the RS data of Figure 4a. The orange/black dotted lines illustrate the cases where solely the transmission/channel number changes along the RS. It is clear that the former process is dominant in the data; that is, the reset transition leaves the junction size similar, and rather the transmission decreases significantly due to the formation of an oxygen-based barrier at the bottleneck. Relying on the extracted  $M$  values, the conductance regime displayed in Figure 4a can be attributed to RS filaments composed of 3–8 Ta atoms in their narrowest cross-section.

## CONCLUSIONS

In conclusion, we utilized superconducting subgap spectroscopy to reveal the microscopic structure of atomic-sized oxide-based RS filaments in their HCS and LCS. We experimentally determined the transmission density function of the open conduction channels supported by the filamentary region. Our results were analyzed in comparison to the reference system of pure Ta atomic wires. In the latter case, the conductance histogram lacks any conductance quantization features due to the presence of partially transmitting channels. Instead, the transmission density function exhibits a broad distribution, which is well described by the universal  $\rho^{\text{RMT}}(\tau)$  density function. The presence of some highly transparent channels is characteristic to this universal transmission distribution, which is sensitively detected by superconducting subgap spectroscopy. In sharp contrast, the highly transparent conduction channels in RS filaments are blocked upon the reset transition. This implies that during reset an extended potential barrier arises at the narrowest cross-section of the filament due to the voltage-induced redistribution of oxygen vacancies or tantalum cations. Meanwhile, the filament diameter is preserved at an estimated configuration involving a few Ta atoms. This finding demonstrates that the reset process is fundamentally different from the atom-by-atom thinning of metallic nanowires, resulting in markedly different quantum transport properties. We argue that the presence of oxygen and the formation of a voltage-tunable transmission barrier at the RS device bottleneck also promote a more gradual crossover between the regimes of highly transmissive filaments and barrier-like transport through disconnected filaments. This contrasts with the case of pure metallic wires, where a sharp transition occurs at the disconnection of the final atom. The former gradual transition in the investigated RS filaments is a beneficial property in artificial neural network applications, where fine-tunable conductance states are required even at the ultimate atomic dimensions.<sup>52</sup>

Furthermore, our analysis demonstrates the merits of quantum transport measurements in the microscopic understanding of atomistic processes in filamentous RS devices. This analysis can be extended to the study of atomistic processes in further RS media in the future, even in on-chip devices. These devices must be in contact with two superconducting

electrodes for subgap analysis. This technique, however, is restricted for memristive devices with an ultrasmall ( $\lesssim 10$  nm) thickness of the active volume between the contacting superconducting electrodes<sup>5</sup> since the thickness of the intrinsically non-superconducting region should not exceed the superconducting coherence length of the electrodes to study the differences in the subgap spectra of various RS states.

## ASSOCIATED CONTENT

### Supporting Information

The Supporting Information is available free of charge at <https://pubs.acs.org/doi/10.1021/acsnm.3c04769>.

RS characteristics of Ta(tip)/Ta<sub>2</sub>O<sub>5</sub>/Ta junctions and on-chip Pt/Ta<sub>2</sub>O<sub>5</sub>/Ta cross-point samples; SEM image of a cross-point sample; multilevel RS in PtIr/Ta<sub>2</sub>O<sub>5</sub>/Ta devices at room temperature; calculated subgap spectra of ScS junctions; measured differential conductance of ScS tunnel junctions comparing pure Ta and Ta/Ta<sub>2</sub>O<sub>5</sub>/Ta systems; role of the transmission density cutoff in the simulated  $I(V)$  curves and histograms; and electric filtering circuitry for simultaneous RS and subgap measurements (PDF)

## AUTHOR INFORMATION

### Corresponding Author

**András Halbritter** – Department of Physics, Institute of Physics, Budapest University of Technology and Economics, H-1111 Budapest, Hungary; HUN-REN-BME Condensed Matter Research Group, H-1111 Budapest, Hungary; [orcid.org/0000-0003-4837-9745](https://orcid.org/0000-0003-4837-9745); Email: [halbritter.andras@ttk.bme.hu](mailto:halbritter.andras@ttk.bme.hu)

### Authors

**Tímea Nóra Török** – Department of Physics, Institute of Physics, Budapest University of Technology and Economics, H-1111 Budapest, Hungary; Institute of Technical Physics and Materials Science, HUN-REN Centre for Energy Research, 1121 Budapest, Hungary; [orcid.org/0000-0001-5238-5895](https://orcid.org/0000-0001-5238-5895)

**Péter Makk** – Department of Physics, Institute of Physics, Budapest University of Technology and Economics, H-1111 Budapest, Hungary; MTA-BME Correlated van der Waals Structures Momentum Research Group, H-1111 Budapest, Hungary

**Zoltán Balogh** – Department of Physics, Institute of Physics, Budapest University of Technology and Economics, H-1111 Budapest, Hungary; HUN-REN-BME Condensed Matter Research Group, H-1111 Budapest, Hungary; [orcid.org/0000-0002-9580-361X](https://orcid.org/0000-0002-9580-361X)

**Miklós Csontos** – Institute of Electromagnetic Fields, ETH Zurich, 8092 Zurich, Switzerland; [orcid.org/0000-0002-2766-6860](https://orcid.org/0000-0002-2766-6860)

Complete contact information is available at: <https://pubs.acs.org/doi/10.1021/acsnm.3c04769>

### Author Contributions

T.N.T. fabricated the cross-point Ta<sub>2</sub>O<sub>5</sub> samples, performed the RS measurements, and did all the data analysis. T.N.T. and P.M. contributed to the measurements on pure Ta atomic wires. M.C. prepared the Ta<sub>2</sub>O<sub>5</sub> layer for STM point-contact measurements. Z.B. contributed to MCBJ sample preparation and supervised the low-temperature measurements. A.H.

conceived the idea of the project and supervised the project. The manuscript was prepared by A.H., T.N.T., and M.C. All authors contributed to the discussion of the results and the manuscript.

## Notes

The authors declare no competing financial interest.

## ACKNOWLEDGMENTS

This research was supported by the Ministry of Culture and Innovation, the National Research, Development and Innovation Office within the Quantum Information National Laboratory of Hungary (grant no. 2022–2.1.1-NL-2022-00004), and the NKFI K143169 grant. Project 963575 of T.N.T. has been implemented with the support provided by the Ministry of Culture and Innovation of Hungary from the National Research, Development and Innovation Fund, financed under the KDP-2020 funding scheme. Z.B. acknowledges the support of the BO/00691/21 Bolyai János Research Scholarship of the Hungarian Academy of Sciences and the ÚNKP-22-5-BME-288 New National Excellence Program of the Ministry for Innovation and Technology from the National Research, Development and Innovation Fund. The cryogenic measurements were supported by the helium liquefaction plant of the BUTE (VEKOP 2.3.3-15-2017-00015), from the European Regional Development Fund. The authors are grateful to G. Zaránd for useful discussions and to G. Rubio-Bollinger for the fitting program based on the theory of multiple Andreev reflections.

## REFERENCES

- (1) Yang, J. J.; Strukov, D. B.; Stewart, D. R. Memristive devices for computing. *Nat. Nanotechnol.* **2013**, *8*, 13–24.
- (2) Zidan, M. A.; Strachan, J. P.; Lu, W. D. The future of electronics based on memristive systems. *Nat. Electron.* **2018**, *1*, 22–29.
- (3) Ambrogio, S.; Narayanan, P.; Tsai, H.; Shelby, R. M.; Boybat, I.; di Nolfo, C.; Sidler, S.; Giordano, M.; Bodini, M.; Farinha, N. C. P.; Killeen, B.; Cheng, C.; Jaoudi, Y.; Burr, G. W. Equivalent-accuracy accelerated neural-network training using analogue memory. *Nature* **2018**, *558*, 60–67.
- (4) Xia, Q.; Yang, J. J. Memristive crossbar arrays for brain-inspired computing. *Nat. Mater.* **2019**, *18*, 309–323.
- (5) Török, T. N.; Csontos, M.; Makk, P.; Halbritter, A. Breaking the Quantum PIN Code of Atomic Synapses. *Nano Lett.* **2020**, *20*, 1192–1200.
- (6) Milano, G.; Aono, M.; Boarino, L.; Celano, U.; Hasegawa, T.; Kozicki, M.; Majumdar, S.; Menghini, M.; Miranda, E.; Ricciardi, C.; Tappertzhofen, S.; Terabe, K.; Valov, I. Quantum Conductance in Memristive Devices: Fundamentals, Developments, and Applications (Adv. Mater. 32/2022). *Adv. Mater.* **2022**, *34*, 2270235.
- (7) Aono, M.; Hasegawa, T. The Atomic Switch. *IEEE Proc.* **2010**, *98*, 2228–2236.
- (8) Cheng, B.; Emboras, A.; Salamin, Y.; Ducry, F.; Ma, P.; Fedoryshyn, Y.; Andermatt, S.; Luisier, M.; Leuthold, J. Ultra compact electrochemical metallization cells offering reproducible atomic scale memristive switching. *Commun. Phys.* **2019**, *2*, 28.
- (9) van Ruitenbeek, J. M.; Morales-Masis, M.; Miranda, E. In *Resistive Switching: From Fundamentals of Nanoionic Redox Processes to Memristive Device Applications* Ch. 7. *Quantum Point Contact Conduction*; Ielmini, D., Waser, R., Eds.; Wiley VCH: Weinheim, 2016; pp 197–224.
- (10) Kittel, C. *Introduction to Solid State Physics*, 8th ed.; John Wiley & Sons, Inc.: New York, 2005.
- (11) van Wees, B. J.; van Houten, H.; Beenakker, C. W. J.; Williamson, J. G.; Kouwenhoven, L. P.; van der Marel, D.; Foxon, C. T. Quantized conductance of point contacts in a two-dimensional electron gas. *Phys. Rev. Lett.* **1988**, *60*, 848–850.
- (12) Agraït, N.; Yeyati, A. L.; van Ruitenbeek, J. M. Quantum Properties of Atomic-Sized Conductors. *Phys. Rep.* **2003**, *377*, 81–279.
- (13) Cuevas, J. C.; Scheer, E. *Molecular Electronics: An Introduction to Theory and Experiment*; World Scientific Series in Nanoscience and Nanotechnology; World Scientific: Singapore, 2010.
- (14) Scheer, E.; Agraït, N.; Cuevas, J. C.; Yeyati, A. L.; Ludoph, B.; Martín-Rodero, A.; Bollinger, G. R.; van Ruitenbeek, J. M.; Urbina, C. The signature of chemical valence in the electrical conduction through a single-atom contact. *Nature* **1998**, *394*, 154–157.
- (15) Park, G.-S.; Kim, Y. B.; Park, S. Y.; Li, X. S.; Heo, S.; Lee, M.-J.; Chang, M.; Kwon, J. H.; Kim, M.; Chung, U.-I.; Dittmann, R.; Waser, R.; Kim, K. In situ observation of filamentary conducting channels in an asymmetric Ta<sub>2</sub>O<sub>5-x</sub>/TaO<sub>2-x</sub> bilayer structure. *Nat. Commun.* **2013**, *4*, 2382.
- (16) Marchewka, A.; Roesgen, B.; Skaja, K.; Du, H.; Jia, C.-L.; Mayer, J.; Rana, V.; Waser, R.; Menzel, S. Nanoionic Resistive Switching Memories: On the Physical Nature of the Dynamic Reset Process. *Adv. Electron. Mater.* **2016**, *2*, 1500233.
- (17) Yang, J. J.; Zhang, M.-X.; Strachan, J. P.; Miao, F.; Pickett, M. D.; Kelley, R. D.; Medeiros-Ribeiro, G.; Williams, R. S. High switching endurance in TaOx memristive devices. *Appl. Phys. Lett.* **2010**, *97*, 232102.
- (18) Torrezan, A. C.; Strachan, J. P.; Medeiros-Ribeiro, G.; Williams, R. S. Sub-nanosecond switching of a tantalum oxide memristor. *Nanotechnology* **2011**, *22*, 485203.
- (19) Strachan, J. P.; Torrezan, A. C.; Medeiros-Ribeiro, G.; Williams, R. S. Measuring the switching dynamics and energy efficiency of tantalum oxide memristors. *Nanotechnology* **2011**, *22*, 505402.
- (20) Lee, M.-J.; Lee, C. B.; Lee, D.; Lee, S.; Chang, M.; Hur, J.; Kim, Y.-B.; Kim, C.-J.; Seo, D.; Seo, S.; Chung, U.-I.; Yoo, I.-K.; Kim, K. A Fast, High-Endurance and Scalable Non-Volatile Memory Device Made from Asymmetric Ta<sub>2</sub>O<sub>5-X</sub>/TaO<sub>2-X</sub> Bilayer Structures. *Nat. Mater.* **2011**, *10*, 625–630.
- (21) Graves, C. E.; Dávila, N.; Merced-Grafals, E. J.; Lam, S.-T.; Strachan, J. P.; Williams, R. S. Temperature and field-dependent transport measurements in continuously tunable tantalum oxide memristors expose the dominant state variable. *Appl. Phys. Lett.* **2017**, *110*, 123501.
- (22) Rao, M.; Song, W.; Kiani, F.; Asapu, S.; Zhuo, Y.; Midya, R.; Upadhyay, N.; Wu, Q.; Barnell, M.; Lin, P.; Li, C.; Wang, Z.; Xia, Q.; Joshua Yang, J. Timing Selector: Using Transient Switching Dynamics to Solve the Sneak Path Issue of Crossbar Arrays. *Small Sci.* **2022**, *2*, 2100072.
- (23) Csontos, M.; Horst, Y.; Olalla, N. J.; Koch, U.; Shorubalko, I.; Halbritter, A.; Leuthold, J. Picosecond Time-Scale Resistive Switching Monitored in Real-Time. *Adv. Electron. Mater.* **2023**, *9*, 2201104.
- (24) Scheer, E.; Joyez, P.; Esteve, D.; Urbina, C.; Devoret, M. H. Conduction Channel Transmissions of Atomic-Size Aluminum Contacts. *Phys. Rev. Lett.* **1997**, *78*, 3535–3538.
- (25) Ludoph, B.; van der Post, N.; Bratus', E. N.; Bezuglyi, E. V.; Shumeiko, V. S.; Wendin, G.; van Ruitenbeek, J. M. Multiple Andreev reflection in single-atom niobium junctions. *Phys. Rev. B: Condens. Matter Phys.* **2000**, *61*, 8561–8569.
- (26) Makk, P.; Csonka, S.; Halbritter, A. Effect of hydrogen molecules on the electronic transport through atomic-sized metallic junctions in the superconducting state. *Phys. Rev. B: Condens. Matter Phys.* **2008**, *78*, 045414.
- (27) Landauer, R. Electrical resistance of disordered one-dimensional lattices. *Philos. Mag.* **1970**, *21*, 863–867.
- (28) Beenakker, C. W. J. Random-matrix theory of quantum transport. *Rev. Mod. Phys.* **1997**, *69*, 731–808.
- (29) Wagenaar, J. J. T.; Morales-Masis, M.; van Ruitenbeek, J. M. Observing “quantized” conductance steps in silver sulfide: Two parallel resistive switching mechanisms. *J. Appl. Phys.* **2012**, *111*, 014302.
- (30) Morales-Masis, M.; Wiemhöfer, H. D.; van Ruitenbeek, J. M. Towards a quantitative description of solid electrolyte conductance switches. *Nanoscale* **2010**, *2*, 2275–2280.

- (31) Ohno, T.; Hasegawa, T.; Tsuruoka, T.; Terabe, K.; Gimzewski, J. K.; Aono, M. Short-term plasticity and long-term potentiation mimicked in single inorganic synapses. *Nat. Mater.* **2011**, *10*, 591–595.
- (32) Lanza, M.; Zhang, K.; Porti, M.; Nafria, M.; Shen, Z. Y.; Liu, L. F.; Kang, J. F.; Gilmer, D.; Bersuker, G. Grain boundaries as preferential sites for resistive switching in the HfO<sub>2</sub> resistive random access memory structures. *Appl. Phys. Lett.* **2012**, *100*, 123508.
- (33) Lanza, M.; Bersuker, G.; Porti, M.; Miranda, E.; Nafria, M.; Aymerich, X. Resistive switching in hafnium dioxide layers: Local phenomenon at grain boundaries. *Appl. Phys. Lett.* **2012**, *101*, 193502.
- (34) Lanza, M. A. A Review on Resistive Switching in High-k Dielectrics: A Nanoscale Point of View Using Conductive Atomic Force Microscope. *Materials* **2014**, *7*, 2155–2182.
- (35) Kurnia, F.; Liu, C.; Liu, G.; Vasudevan, R. K.; Yang, S. M.; Kalinin, S. V.; Valanoor, N.; Hart, J. N. Localised nanoscale resistive switching in GaP thin films with low power consumption. *J. Mater. Chem. C* **2017**, *5*, 2153–2159.
- (36) Wedig, A.; Luebben, M.; Cho, D.-Y.; Moors, M.; Skaja, K.; Rana, V.; Hasegawa, T.; Adepalli, K. K.; Yildiz, B.; Waser, R.; Valov, I. Nanoscale cation motion in TaO<sub>x</sub>, HfO<sub>x</sub> and TiO<sub>x</sub> memristive systems. *Nat. Nanotechnol.* **2016**, *11*, 67–74.
- (37) Moors, M.; Adepalli, K. K.; Lu, Q.; Wedig, A.; Bäumer, C.; Skaja, K.; Arndt, B.; Tuller, H. L.; Dittmann, R.; Waser, R.; Yildiz, B.; Valov, I. Resistive Switching Mechanisms on TaO<sub>x</sub> and SrRuO<sub>3</sub> Thin-Film Surfaces Probed by Scanning Tunneling Microscopy. *ACS Nano* **2016**, *10*, 1481–1492.
- (38) Valov, I.; Sapezanskaia, I.; Nayak, A.; Tsuruoka, T.; Bredow, T.; Hasegawa, T.; Staikov, G.; Aono, M.; Waser, R. Atomically controlled electrochemical nucleation at superionic solid electrolyte surfaces. *Nat. Mater.* **2012**, *11*, 530–535.
- (39) Santa, B.; Balogh, Z.; Pósa, L.; Krisztian, D.; Török, T. N.; Molnár, D.; Sinkó, C.; Hauert, R.; Csontos, M.; Halbritter, A. Noise Tailoring in Memristive Filaments. *ACS Appl. Mater. Interfaces* **2021**, *13*, 7453–7460.
- (40) Santa, B.; Molnár, D.; Haiber, P.; Gubicza, A.; Szilágyi, E.; Zolnai, Z.; Halbritter, A.; Csontos, M. Nanosecond resistive switching in Ag/AgI/PtIr nanojunctions. *Beilstein J. Nanotechnol.* **2020**, *11*, 92–100.
- (41) Santa, B.; Balogh, Z.; Gubicza, A.; Pósa, L.; Krisztian, D.; Mihály, G.; Csontos, M.; Halbritter, A. Universal 1/f type current noise of Ag filaments in redox-based memristive nanojunctions. *Nanoscale* **2019**, *11*, 4719–4725.
- (42) Molnár, D.; Török, T. N.; Santa, B.; Gubicza, A.; Magyarkuti, A.; Hauert, R.; Kiss, G.; Halbritter, A.; Csontos, M. In situ impedance matching in Nb/Nb<sub>2</sub>O<sub>5</sub>/PtIr memristive nanojunctions for ultra-fast neuromorphic operation. *Nanoscale* **2018**, *10*, 19290–19296.
- (43) Gubicza, A.; Manrique, D. Z.; Pósa, L.; Lambert, C. J.; Mihály, G.; Csontos, M.; Halbritter, A. Asymmetry-induced resistive switching in Ag-Ag<sub>2</sub>S-Ag memristors enabling a simplified atomic-scale memory design. *Sci. Rep.* **2016**, *6*, 30775.
- (44) Gubicza, A.; Csontos, M.; Halbritter, A.; Mihály, G. Non-exponential resistive switching in Ag<sub>2</sub>S memristors: a key to nanometer-scale non-volatile memory devices. *Nanoscale* **2015**, *7*, 4394–4399.
- (45) Gubicza, A.; Csontos, M.; Halbritter, A.; Mihály, G. Resistive switching in metallic Ag<sub>2</sub>S memristors due to a local overheating induced phase transition. *Nanoscale* **2015**, *7*, 11248–11254.
- (46) Geresdi, A.; Csontos, M.; Gubicza, A.; Halbritter, A.; Mihály, G. A fast operation of nanometer-scale metallic memristors: highly transparent conductance channels in Ag<sub>2</sub>S devices. *Nanoscale* **2014**, *6*, 2613–2617.
- (47) Miao, F.; Strachan, J. P.; Yang, J. J.; Zhang, M.-X.; Goldfarb, I.; Torrezan, A. C.; Eschbach, P.; Kelley, R. D.; Medeiros-Ribeiro, G.; Williams, R. S. Anatomy of a Nanoscale Conduction Channel Reveals the Mechanism of a High-Performance Memristor. *Adv. Mater.* **2011**, *23*, 5633–5640.
- (48) Kaniselvan, M.; Luisier, M.; Mladenović, M. An Atomistic Model of Field-Induced Resistive Switching in Valence Change Memory. *ACS Nano* **2023**, *17*, 8281–8292.
- (49) Xiao, B.; Yu, X.; Watanabe, S. A Comparative Study on the Diffusion Behaviors of Metal and Oxygen Ions in Metal-Oxide-Based Resistance Switches via ab Initio Molecular Dynamics Simulations. *ACS Appl. Electron. Mater.* **2019**, *1*, 585–594.
- (50) Xiao, B.; Watanabe, S. Oxygen vacancy effects on an amorphous-TaO<sub>x</sub>-based resistance switch: a first principles study. *Nanoscale* **2014**, *6*, 10169–10178.
- (51) Xiao, B.; Gu, T.; Tada, T.; Watanabe, S. Conduction paths in Cu/amorphous-Ta<sub>2</sub>O<sub>5</sub>/Pt atomic switch: First-principles studies. *J. Appl. Phys.* **2014**, *115*, 034503.
- (52) Rao, M.; Tang, H.; Wu, J.; Song, W.; Zhang, M.; Yin, W.; Zhuo, Y.; Kiani, F.; Chen, B.; Jiang, X.; Liu, H.; Chen, H.-Y.; Midya, R.; Ye, F.; Jiang, H.; Wang, Z.; Wu, M.; Hu, M.; Wang, H.; Xia, Q.; Ge, N.; Li, J.; Yang, J. J. Thousands of conductance levels in memristors integrated on CMOS. *Nature* **2023**, *615*, 823–829.
- (53) Prezioso, M.; Merrih-Bayat, F.; Hoskins, B. D.; Adam, G. C.; Likharev, K. K.; Strukov, D. B. Training and operation of an integrated neuromorphic network based on metal-oxide memristors. *Nature* **2015**, *521*, 61–64.
- (54) Li, C.; Hu, M.; Li, Y.; Jiang, H.; Ge, N.; Montgomery, E.; Zhang, J.; Song, W.; Dávila, N.; Graves, C. E.; Li, Z.; Strachan, J. P.; Lin, P.; Wang, Z.; Barnell, M.; Wu, Q.; Williams, R. S.; Yang, J. J.; Xia, Q. Analogue signal and image processing with large memristor crossbars. *Nat. Electron.* **2017**, *1*, 52–59.
- (55) Jiang, H.; Li, C.; Zhang, R.; Yan, P.; Lin, P.; Li, Y.; Yang, J. J.; Holcomb, D.; Xia, Q. A provable key destruction scheme based on memristive crossbar arrays. *Nat. Electron.* **2018**, *1*, 548–554.
- (56) Li, C.; Wang, Z.; Rao, M.; Belkin, D.; Song, W.; Jiang, H.; Yan, P.; Li, Y.; Lin, P.; Hu, M.; Ge, N.; Strachan, J. P.; Barnell, M.; Wu, Q.; Williams, S.; Yang, J. J.; Xia, Q. Long short-term memory networks in memristor crossbar arrays. *Nat. Mach. Intell.* **2019**, *1*, 49–57.
- (57) Wang, Z.; Li, C.; Song, W.; Rao, M.; Belkin, D.; Li, Y.; Yan, P.; Jiang, H.; Lin, P.; Hu, M.; Strachan, J. P.; Ge, N.; Barnell, M.; Wu, Q.; Barto, A. G.; Qiu, Q.; Williams, S.; Xia, Q.; Yang, J. J. Reinforcement learning with analogue memristor arrays. *Nat. Electron.* **2019**, *2*, 115–124.
- (58) Li, C.; Belkin, D.; Li, Y.; Yan, P.; Hu, M.; Ge, N.; Jiang, H.; Montgomery, E.; Lin, P.; Wang, Z.; Song, W.; Strachan, J. P.; Barnell, M.; Wu, Q.; Williams, R. S.; Yang, J. J.; Xia, Q. Efficient and self-adaptive in-situ learning in multilayer memristor neural networks. *Nat. Commun.* **2018**, *9*, 2385.
- (59) Hu, M.; Graves, C.; Li, C.; Li, Y.; Ge, N.; Montgomery, E.; Davila, N.; Jiang, H.; Williams, S.; Yang, J. J.; Xia, Q.; Strachan, J. P. Memristor-Based Analog Computation and Neural Network Classification with a Dot Product Engine. *Adv. Mater.* **2018**, *30*, 1705914.
- (60) Henny, M.; Oberholzer, S.; Strunk, C.; Schönenberger, C. 1/3-shot-noise suppression in diffusive nanowires. *Phys. Rev. B: Condens. Matter Mater. Phys.* **1999**, *59*, 2871–2880.
- (61) Riquelme, J. J.; Vega, L. d. l.; Yeyati, A. L.; Agrait, N.; Martín-Rodero, A.; Rubio-Bollinger, G. Distribution of conduction channels in nanoscale contacts: Evolution towards the diffusive limit. *Europhys. Lett.* **2005**, *70*, 663–669.
- (62) Cuevas, J. C.; Yeyati, A. L.; Martín-Rodero, A. Microscopic Origin of Conducting Channels in Metallic Atomic-Size Contacts. *Phys. Rev. Lett.* **1998**, *80*, 1066–1069.
- (63) Vardimon, R.; Klionsky, M.; Tal, O. Indication of complete spin filtering in atomic-scale nickel oxide. *Nano Lett.* **2015**, *15*, 3894–3898.
- (64) Nazarov, Y. V. Limits of universality in disordered conductors. *Phys. Rev. Lett.* **1994**, *73*, 134–137.
- (65) Cuevas, J. C.; Martín-Rodero, A.; Yeyati, A. L. Hamiltonian approach to the transport properties of superconducting quantum point contacts. *Phys. Rev. B: Condens. Matter Mater. Phys.* **1996**, *54*, 7366–7379.
- (66) Averin, D.; Bardas, A. ac Josephson Effect in a Single Quantum Channel. *Phys. Rev. Lett.* **1995**, *75*, 1831–1834.

(67) Senkpiel, J.; Drost, R.; Klöckner, J. C.; Etzkorn, M.; Ankerhold, J.; Cuevas, J. C.; Pauly, F.; Kern, K.; Ast, C. R. Extracting transport channel transmissions in scanning tunneling microscopy using superconducting excess current. *Phys. Rev. B: Condens. Matter Mater. Phys.* **2022**, *105*, 165401.

(68) Levy, M.; Rudnick, I. Ultrasonic Determination of the Superconducting Energy Gap in Tantalum. *Phys. Rev.* **1963**, *132*, 1073–1080.

(69) Vardimon, R.; Matt, M.; Nielaba, P.; Cuevas, J. C.; Tal, O. Orbital origin of the electrical conduction in ferromagnetic atomic-size contacts: Insights from shot noise measurements and theoretical simulations. *Phys. Rev. B: Condens. Matter Mater. Phys.* **2016**, *93*, 085439.